Mapping reaction mechanism during overcharge of a LiNiO2/graphite–silicon lithium-ion battery: a correlative *operando* approach by simultaneous gas analysis and synchrotron scattering techniques

Quentin Jacquet, Irina Profatilova, Loïc Baggetto, Bouthayna Alrifai, Elisabeth Addes, Paul Chassagne, Nils Blanc, Samuel Tardif, Lise Daniel, Sandrine Lyonnard

ADVANCED ENERGY MATERIALS
www.advenergymat.de

Mapping Reaction Mechanism During Overcharge of a $LiNiO_2$/Graphite–Silicon Lithium-Ion Battery: A Correlative *Operando* Approach by Simultaneous Gas Analysis and Synchrotron Scattering Techniques

Quentin Jacquet, Irina Profatilova, Loïc Baggetto, Bouthayna Alrifai, Elisabeth Addes, Paul Chassagne, Nils Blanc, Samuel Tardif, Lise Daniel, and Sandrine Lyonnard**

Li-ion battery degradation processes are multi-scale, heterogeneous, dynamic, and depend on the battery usage. Degradation mechanisms during overcharge of $LiNiO_2$ are well known at the material level featuring O_2 gas release and concomitant surface reconstruction of $LiNiO_2$. However, there are still debates regarding the role of the high voltage phase formation, so called O1, on gas production. Moreover, little information is available on the effect of produced gases on the cell components (anode or sensors), or the effect of overcharge on electrode level behavior. In this work, we simultaneously measure the gas evolution using *operando* mass spectrometry while spatially resolving nanostructure and crystallographic lattice parameter changes using *operando* micro small/wide angle X-ray scattering (SAXS/WAXS) mapping during the formation and overcharge of a $LiNiO_2$/Graphite—Silicon pouch cell. This new correlated *operando* characterization experiment allowed to (1) confirm the absence of O1 phase even with substantial gas produced at end of charge, (2) unveil the effect of gases on reference electrode and (3) show that overcharge increases in-plane reaction heterogeneities by creating local degraded regions lagging behind the ensemble electrochemistry. These findings will be important to optimize ageing of devices based on similar chemistries, in particular Ni-rich cathodes, while showing the strength of correlated characterization leading to more efficient and robust information on complex mechanisms.

1. Introduction

The widespread development of electrical vehicles needed for the electrification of the transportation sector will require mining and refining very large quantities of raw materials, some of these being scarce or geographically concentrated.[1,2] Increasing lifetime and energy density of lithium-ion batteries (LIBs) is therefore crucial to reduce the number of batteries that need to be produced and recycled, as well as to extend the driving range and minimize the environmental impact of the other materials (packaging, engine, wiring, etc.).

$LiNiO_2$ (LNO) and Graphite–Silicon composite (Gr—Si) are promising materials for high-energy-density Li-ion batteries (LIBs).[3] LNO is the end member of the Ni-rich layered oxide family of general composition $LiNi_xMn_yCo_zO_2$ so called NMC (with $x + y + z = 1$ and $x \geq 0.6$). These Ni-rich materials offer the dual benefit of high energy density and low Co content but suffer from higher degradation upon cycling. In particular,

Q. Jacquet, S. Lyonnard
Univ. Grenoble Alpes
CEA
CNRS
Grenoble INP
IRIG
SyMMES
Grenoble 38000, France
E-mail: quentin.jacquet@cea.fr; sandrine.lyonnard@cea.fr

I. Profatilova, L. Baggetto, B. Alrifai, E. Addes, P. Chassagne, L. Daniel
Univ. Grenoble Alpes
CEA
Liten
DEHT
Grenoble 38000, France

N. Blanc
Univ. Grenoble Alpes
CNRS
Grenoble INP
Institut Néel
Grenoble 38000, France

S. Tardif
University Grenoble Alpes
CEA
CNRS
IRIG
MEM
Grenoble 38000, France

The ORCID identification number(s) for the author(s) of this article can be found under https://doi.org/10.1002/aenm.202404080

DOI: 10.1002/aenm.202404080

(1) lattice oxygen is partially released at high voltage causing surface reconstruction, electrolyte decomposition, and gas evolution leading to battery safety risks[4] and (2) severe intra-particle strains, arising from large unit cell parameter changes during cycling, give rise to particle fracture creating disconnected particles and newly exposed surfaces to the electrolyte.[5] On the anode side, graphite has been used for decades in Li-ion batteries, and Gr—Si, which features a higher energy density compared to graphite thanks to the alloying reaction between Li and Si, also suffers from poorer cycling stability. This originates partly in the failure of the in situ formed passivating film (SEI, solid electrolyte interphase) upon repeated volume expansion/shrinkage of Si particles, leading to constant electrolyte consumption at the anode surface.[6] Anode-side and cathode-side degradations cannot only be studied separately as decomposition products formed at one electrode often lead to gaseous or dissolved species that migrate in the battery and react with other cell components, a process commonly referred to as "crosstalk".[7] Moreover, LIB degradation processes can depend on active material position in the cell and local defects. Indeed, it is known that electrode edges and/or active material areas around defects can have different states of charge (SoC) or reaction kinetics compared to the average electrode reaction, hence different degradation mechanisms.[8,9] Finally, degradation depends also on battery usage, with fast charging or overcharge being particularly harsh conditions.[10] Clearly, degradation mechanisms in Li-ion batteries, and in particular batteries containing LNO/Gr—Si, are very complex because numerous, dynamic, occurring over multiple length scales and involving multiple components.[11] While a consensus on specific degradation mechanisms starts to emerge at the material level, as described earlier for Ni-rich materials or Gr—Si, much work is still needed to (1) spatially resolve degradation processes at the material and cell level, and to (2) understand the correlation between different degradation mechanisms. For example, it is important to unravel interdependencies between cathode/anode phenomena, interactions between gaseous/soluble/solid species, or distribution of active/defective zones in batteries in nominal and abusive conditions.

Along that line, we focus on understanding the correlations between the structural evolution of LNO/Gr—Si and gas release in a full cell especially during the formation cycle and overcharge at 5 V versus Li^+/Li. Moreover, we want to evaluate the spatial homogeneity of structural evolution, especially during overcharge. No single technique can measure all these processes, hence to address these questions, *operando* multi-probe characterization is necessary.[12] It can be done according to two general strategies being (1) carrying out several individual characterizations to measure specific parameters or (2) developing new instruments/techniques capable of measuring simultaneously as many key parameters as possible.[13,14] While the first approach is easier to execute, it holds a major challenge which is to precisely correlated data coming from two different experiments (different *operando* cells, different samples). The second strategy is more ideal since it delivers information on the same sample, in the same cell and at the same time, but it requires developing instruments and *operando* electrochemical cells accommodating several probes. Focusing on the correlation between degassing and structural evolution of the active material, De Biasi et al. applied the first approach and measured in parallel averaged structural evolution in LNO/Li systems up to 4.5 V using *operando* laboratory X-ray diffraction (XRD) on pouch cell and gas formation measured with Online Electrochemical Mass Spectrometry (OEMS) using a different specially designed cell for both experiments.[15] Structure wise, De Biasi et al. observed the classical sequence of H1 → M → H2 → H3 phase transitions in general agreement with literature.[16,17] All H phases are hexagonal phases having the same layered structure but with different cell parameters while M is a monoclinic distortion of these hexagonal phases. There are still debates on the formation mechanism of the O1 phase at the end of charge observed in some but not all reports and suggested to be related to O_2 loss.[18,19] O1 phase is also an hexagonal layered phase similar to the other H phases but with a different oxygen stacking, as detailed by Xu et al.[17] In terms of gas release, they observed the formation of CO_2 at 4.1 V versus Li^+/Li corresponding to the onset of the H2 → H3 transition in LNO while O_2 is mostly produced after this transition. Other reports mentioned CO_2 onset at 3.8 V or 4.4 V with or without the presence of O_2.[20,21] To the best of our knowledge, there is no report of simultaneous *operando* gas measurements and structural evolution of active materials during cycling (same sample, same cell, same time) in LIBs. Turning to resolving in-plane heterogeneities during cycling, XRD imaging has been used to locate Li plating during fast charge in single-layer pouch cells or ageing in prismatic cells for NMC/Gr—Si systems.[22–24] Moreover, XRD imaging of a NMC/Gr pouch cell during formation cycle revealed massive heterogeneities that the authors attributed to gas formation.[25] However, there is no information available in general regarding the relationship between overcharge and cell level reaction heterogeneity.

The present work reports the simultaneous measurements of gases and mapping of active material structural evolution in a single layer pouch cell during formation and overcharge cycles. The LNO/Gr—Si pouch cell is connected to a mass spectrometer and entirely scanned with a synchrotron X-ray microbeam during cycling to measure the time-resolved wide angle and small angle X-ray scattering (WAXS and SAXS) patterns. First, by comparing the obtained data with literature and other lab-based experiments, we confirm the validity of our new challenging experimental set-up, now available to the battery community. Second, we obtain a direct correlation between the averaged structural evolution of the LNO and Gr materials determined by diffraction (WAXS) and the gas released. With this correlation, we find, for example, that CO_2 and O_2 are released only at the end of the H2-H3 transition without noticeable bulk O1 phase formation in LNO. Third, we quantify the in-plane heterogeneities in both electrodes by spatially resolving the lattice parameter changes. The observed heterogeneities are found to originate from three main sources – (1) edge effects due to oversized Gr—Si electrode, (2) reference electrode, and (3) the gases generated during overcharge. Indeed, the discharge after the overcharge features very local spots (smaller than the mm) lagging behind the overall electrochemistry. Some of these positions correspond to visible fabrication defects of the pouch cell. We propose that gas bubbles formed during the overcharge gather and grow at cell defects inducing the observed heterogeneity.

2. Results

2.1. Proof of Concept of the Multi-Technique Experiment

The experiment consists in imaging the active material (de)lithiation in *operando* conditions inside a single-layer LNO/Gr—Si pouch cell while simultaneously following gas generation (**Figure 1**a). For that purpose, a 10 × 8 cm^2 pouch cell containing a 2.3 × 2.3 cm^2 positive electrode is connected to a mass spectrometer through a gas analysis line continuously purged with Ar carrier gas allowing the chemical analysis of gases produced. Simultaneously, the entire electrode stack is scanned using a 65 × 100 μm^2 X-ray beam mapping a zone of 3 × 3 cm^2 (Figure 1b). Wide and small angle scattering patterns are recorded simultaneously every 1 mm in the cell to resolve the atomic structure evolution of LNO and Gr with WAXS while probing information on the nanoscale using SAXS. These maps are recorded in 6 min and ≈200 maps per cycle were acquired, which corresponds to ≈1% capacity change per map. A formation cycle up to 4.2 V at C/13 and overcharge cycle up to 5 V at C/9 were successively measured. Both conditions are known to produce gases due to SEI formation and decomposition of cathode material together with electrolyte oxidation at high voltage.

Charge and discharge voltage profiles for both cycles are composed of several plateaus corresponding to the various well-known transitions during (de)lithiation of LNO and Gr—Si electrodes (Figure 1c).[3,26] At the end of the formation and overcharge, the capacity reaches 196 mAh g^{-1}_{LNO} which is in agreement with previous reports on the same chemistry.[3] Note that the electrochemical profile is almost identical to similar pouch cells measured in the lab and in absence of X-ray beam (Figure S2, Supporting Information). The pouch cell is equipped with a $LiFePO_4/FePO_4$ (LFP/FP) reference electrode to access the individual voltage of both positive and negative electrodes. When looking at the individual voltages, an important drop of the cathode and anode voltage during the 5 V (cell voltage) hold is observed for the cell tested at the beamline (Figure S2c,e, Supporting Information). In addition, subsequent to the 5 V hold, there is a drop of voltage of ≈0.4 V at the beginning of the second discharge for both electrodes. The origin of this drop is nested in Li removal from the LFP of the reference electrode during the hold at 5 V, and is expected to increase the reference potential from 3.42 V up to ≈3.8 V versus Li^+/Li. Removal of Li was quantified *operando* from the LFP/FP phase fraction obtained by WAXS and ex situ by *post mortem* electrochemical analysis (Figures S3 and S4, Supporting Information). The concentration change (quasi-complete delithiation of LFP into FP) led to the temporary increase of the reference electrode potential, which shows that the measured cathode and anode voltage drops are not due to actual changes in electrochemical potential of active electrodes. We hypothesize that LFP is chemically delithiated by gases formed during overcharge (CO_2 and O_2).[27] Turning to the WAXS signal, diffraction peaks of LNO and Gr are clearly visible on the spatially averaged WAXS patterns shown in Figure 1c. The (111) Si peak at 2 $Å^{-1}$ is barely visible due to the small fraction of crystalline Si in the electrode (11 wt.%) and its nanometric size (30 nm) (Figures S5–S6, Supporting Information). For LNO, the peak around 1.3 $Å^{-1}$ corresponds to the (003) reflection of LNO (R-*3 m*) and is indicative of the interlayer distance between the NiO_2 slabs of this layered material. It shifts toward lower Q values (larger interlayer distance) at the beginning of charge and higher Q values (smaller interlayer distances) at the end of charge with a strong shift at the very end corresponding to the formation of the so-called H3 phase.[17] Moving to the anode side, peaks in the region between 1.75–1.95 $Å^{-1}$ are indicative of the presence and interlayer distance of graphite and lithiated compounds Li_xC_6. Typical reported phase sequence during lithiation features graphite (≈1.87 $Å^{-1}$), Stage X for X > 3 (≈1.85 $Å^{-1}$), Stage 3L - $Li_{0.2}C_6$ (≈1.81 $Å^{-1}$), Stage 2L/2 - $Li_{0.33}C_6/Li_{0.5}C_6$ (≈1.79 $Å^{-1}$), and Stage 1 corresponding to LiC_6 (≈1.70 $Å^{-1}$).[28] Overall, the evolution of LNO and Gr diffraction peaks during charge and discharge follows similar trend to reported work.[29] The gas evolution profiles measured during cycling at the ESRF and in the lab (without X-ray exposure) using OEMS are compared in Figures S9 and S10 (Supporting Information). The data obtained in the lab feature a slightly better signal for some gases due to lower baselines thanks to a more efficient purge of the cell and line prior to the electrochemical tests. Nonetheless, the gas evolution trends are essentially the same for both cells, confirming the absence of beam effect on gas production even at high voltage where the electrochemical decomposition of the electrolyte occurs. Altogether, we have established a proof of concept of a functioning experiment combining OEMS with fast synchrotron microbeam WAXS/SAXS mapping free of beam damage effects (in agreement to the dose calculations, see experimental details).

2.2. Reaction Mechanism During Formation Cycle

Next, we will discuss a quantitative analysis starting with the formation cycle. Interlayer distance for Li_xC_6, *c* parameter for LNO, and normalized SAXS integrated intensity between 4.10^{-3} and 3.10^{-2} $Å^{-1}$ (Figure S11, Supporting Information) are calculated at different pixel positions in the pouch cell and plotted together with the gas signal and the voltage profile on **Figure 2**. Graphite interlayer distance increases from the beginning of charge with a strong heterogeneity depending on the position in the pouch cell. Indeed, graphite not directly facing LNO (green) lithiates to a lesser extent than the edges (purple) and center (orange), which is expected due to the oversized Gr—Si electrode compared to LNO. During discharge, almost full graphite delithiation is achieved at the middle of discharge suggesting that only Si delithiation occurs in the second half of discharge. During the 1st charge, the intensity of the crystalline Si peak decreases continuously by up to 35% (Figures S5 and S6, Supporting Information), which is consistent with the crystalline to amorphous transition during Si lithiation and shows the continuous participation of Si during charge. Peaks attributed to $Li_{15}Si_4$, the crystalline end-member of the electrochemical Li-Si system, are not evidenced, supporting the incomplete reaction of Si and its participation within an amorphous phase. No changes in the Si peak intensity is observed during discharge showing that the reacted silicon remains amorphous after delithiation. This is a characteristic of Gr—Si electrodes, for which there is a simultaneous lithiation of graphite and silicon during the first lithiation, and a sequential delithiation with graphite being the first to delithiate.[14] The relatively low lithiation of Si (only 35% of reacted crystalline Si)

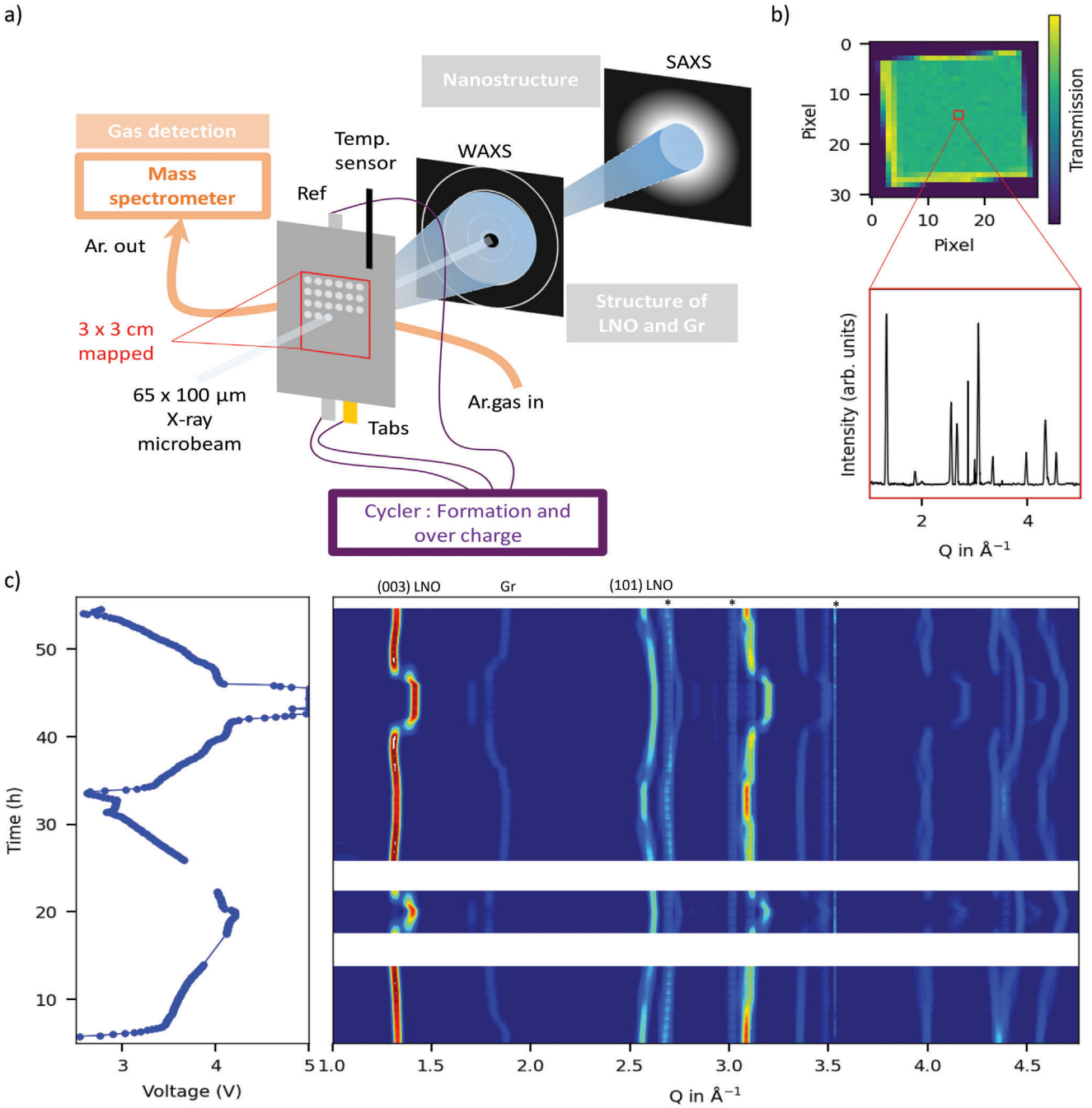

Figure 1. Principle of the *operando* correlated SAXS/WAXS mapping & OEMS experiment a) schematic of the experimental set-up, b) 2D transmission map of the electrode stack – the center (green) region corresponds to the LNO/Gr—Si stack while the yellow borders are the region where only the oversized Gr—Si is present. Contours of the electrode stack appear dark because of stainless steel sample holder. Pixel size is 1 × 1 mm. Each pixel contains a full WAXS (inset at the bottom) pattern and a SAXS pattern. c) Electrochemical data during the formation and overcharge together a colormap representing the evolution of the WAXS patterns (each pattern is spatially averaged over the entire electrode stack). Color corresponds to the WAXS intensity. Background and peaks from current collectors were removed during the data analysis. * mark the position of the current collector peak residuals while most of the peaks above 3 Å^{-1} come from LNO. White stripes correspond to beam loss regions.

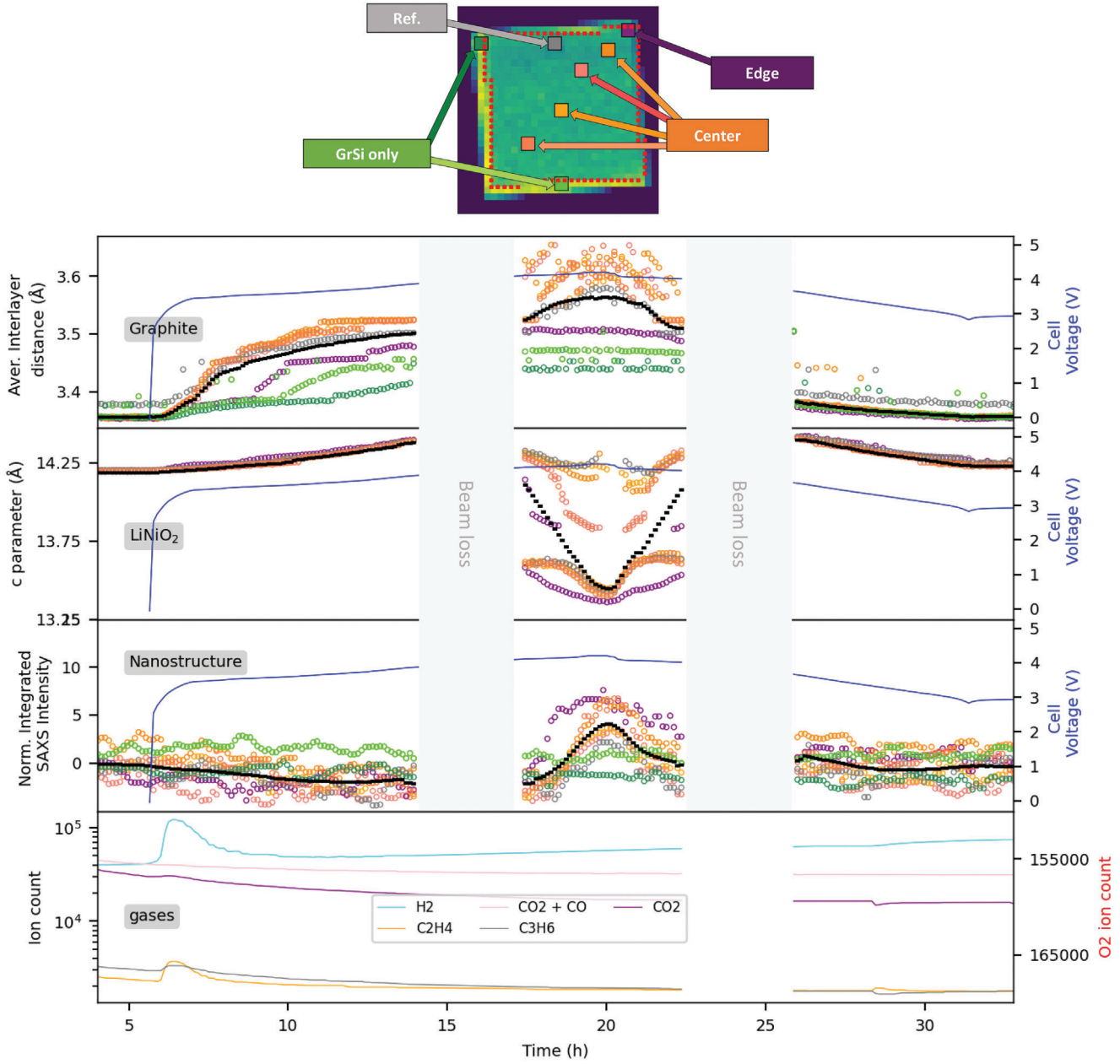

Figure 2. Structural changes and gas formation during the formation cycle. From top to bottom, evolution during formation cycle of the interlayer distance in Li_xC_6, c parameter of Li_xNiO_2, SAXS integrated intensity, gas evolution for specific fragments. For all these graphs (apart for the gas analysis), different positions in the pouch cell are shown namely center, reference electrode, edge, and Gr—Si only in orange, brown, purple, and green respectively. Black curve corresponds to the average over the entire electrode while the blue curve represents the full cell voltage profile. At the top of the graph, a 2D transmission map of the pouch cell showing selected pixel positions in the pouch cell together with the borders of the LNO electrode (red dotted line). Vertical grey dotted line is a guide to the eye marking the end of the charge.

is surprising, and we hypothesize that the large available anode surface (and hence the large amount of available graphite particles) together with the well-known activation energy required to lithiate crystalline silicon might be responsible for its lower than expected participation.[30] For the LNO, the increase and decrease of *c* parameter during charge appears much more homogenous over the pouch cell with the exception of the H2 → H3 transition, corresponding to the rapid decrease of *c* (for the corresponding change in unit cell volume see Figure S7, Supporting Information). Indeed, while the edges are the first to undergo complete H2 → H3 transition, LNO at the reference electrode position still contains H2 after reaching 4.2 V. Delithiation occurs symmetrically to the lithiation. Regarding SAXS data, as the intensity scales as the electronic density and volume of scatterers (See Figure S8, Supporting Information), it is very sensitive to local heterogeneities in mass loadings and positions probed in the

cell. Therefore, Figure 2 shows the SAXS integrated intensity subtracted from the intensity at the OCV, called normalized SAXS integrated intensity. It remains constant during the formation cycle apart from a reversible increase at the end of charge for the edge and center position. Considering the strong SAXS intensity originating from LNO (Figure S8, Supporting Information) and the good correlation between *c* parameter change of LNO and SAXS integrated intensity increase, we hypothesize that the SAXS signal is dominated by LNO electrode evolution, potentially linked to the rapid increase of LNO density due to the decrease of the unit cell volume. Gas evolution during formation cycle features H_2 and C_2H_4 which are observed at the beginning of the first charge along with contributions from CO_2 and C_3H_6 (Figures S9 and S10, Supporting Information) corresponding to the SEI formation.[31] A pronounced CO_2 formation at the beginning of charge in Figure S10d (Supporting Information) corresponds to the SEI layer formation and to surface Li_2CO_3 oxidation for LNO, in agreement with literature data.[32,33] A small CO_2 signal is observed in the lab experiment in Figure S10d (Supporting Information) (not visible during the synchrotron experiment) at the very end of the first charge and at the beginning of discharge likely due to reactive oxygen release from LNO material and reaction with electrolyte as reported previously.[15]

2.3. Reaction Mechanism During Overcharge

Turning to the overcharge, similar metrics have been extracted and are shown **Figure 3**. The general structural evolution during overcharge is similar to the formation cycle with, however a few differences, described and discussed in the following. Focusing first on graphite, lithiation does not start at the beginning of charge but after 2.5 h (at C/9). This results from the lithiation of amorphous silicon formed at the end of the 1st discharge which occurs at higher potential vs Li^+/Li compared to graphite.[34] At 5 V, there is strong heterogeneity in the interlayer distance across the pouch cell. During the 5 V hold (3h), the heterogeneity does not evolve while the average interlayer distance decreases very slightly suggesting partial delithiation. One of the possible explanations for this delithiation can be the reaction of intercalated lithium with CO_2, as also observed for LFP reference electrode.[35,36] Another possible explanation is a reaction between lithiated graphite and remaining crystalline Si as evidenced by Berhaut et al. during relaxation.[30] Unfortunately, this is difficult to quantify due to the low Si peak intensity. During discharge, and despite the hold, graphite interlayer distance reversibly gets back to initial values, and as observed during the formation cycle, graphite almost fully delithiates during the first half of discharge. For LNO, at 4.3 V, the average *c* parameter reaches 13.34 Å with little in plane heterogeneity indicative of complete H2 → H3 transition. During 5 V hold, the average *c* parameter for LNO decreases slightly showing signs of bulk modification during the hold which could be related to delithiation of the last Li ions having slow diffusion.[37] However, no trace of O1 phase formation was observed (Figure S13, Supporting Information). During discharge, the average *c* parameter reverts to its original value and for some central position, the H3 phase is observed over a wider voltage range compared to the charge (this will be discussed in more details in next sections).

The overcharge gas evolution is Figure 3d; Figure S9 and S10 not described for LNO/Gr—Si cells in the literature yet. There is a massive gas evolution starting at the end of the H2 – H3 transition concomitant with rapid voltage raise (Figure S9 and S10, Supporting Information). CO_2, CO and O_2 are produced by the positive electrode side at high voltage. This finding has been confirmed by a specially designed OEMS experiment where a pouch cell containing LNO positive and delithiated $FePO_4$ negative electrodes were used, see Figure S12 (Supporting Information). CO_2, CO, and O_2 probably result fromthe chemical oxidation of the electrolyte via lattice oxygen as described earlier, as well as from the direct oxidation of ethylene carbonate, FEC and carbon black at voltages >4.7 V versus Li/Li^+.[38,4,39] Note that traces of HF were detected during a 5 V hold at m/z = 19, which supports the mechanism of electrochemical oxidation of EC and its subsequent reaction with PF_6^- anion.[40] The other gasses observed, that is, H_2, CH_4, C_2H_4, and C_3H_6 originate from the reductive decomposition of the electrolyte at the negative electrode at low potentials. The presence of these gasses is unexpected as the negative electrode is assumed to be passivated by a SEI layer. Presence of Li plating is ruled out by the high negative/positive electrode loading (N/P) ratio of ca. 1.5 used in this study and the absence of Li metal peaks in the diffraction patterns. The formation of hydrocarbons is therefore indicative of constant SEI formation and breakdown which might originate from the presence of HF and/or gasses formed at the cathode damaging the SEI. Note that the amount of formed hydrocarbons is higher than during the SEI formation hence the observed gas evolution is likely not due to the residual lithiation of amorphous Si. *Post mortem* gas chromatography - mass spectrometry (GC-MS), analysis of the electrolyte for the cells tested at the synchrotron and in the laboratory revealed considerable consumption of FEC for both cells and in situ formation of vinylene carbonate (VC) after cycling (Figure S14 and Table S1, Supporting Information). Conversion of FEC to VC was described previously by Etacheri et al. which was associated with HF formation.[41] After ≈1 h of 5 V hold, there is an increase of C_2H_4 production together with a decrease of the O_2, H_2 and CO_2 gas production which remains constant for the last 2 h of the hold. This decrease could be related to a passivation of the LNO oxide surface. This result agrees partially with the data reported by Papp et al.[42] in which CO_2 evolution quickly diminished during a 5 V hold for LNO. The concomitant increase of C_2H_4 and decrease of O_2 can be explained by the exothermic reaction of C_2H_4 with O_2 forming CO_2.[35] Some of the above-mentioned hypotheses are confirmed by the difference in total amounts of gases generated by LNO/delithiated LFP and LNO/Gr—Si cells during the overcharge cycles. Figure S12d (Supporting Information) demonstrates larger amounts of CO_2 and CO produced when Gr—Si electrode was used as well as the absence of H_2 and other hydrocarbons for LFP negative electrode. Increased CO_2 production for LNO/Gr—Si cell may come from FEC reduction at low potential and from partial conversion of C_2H_4 to CO_2 in reactions with oxygen.[35]

SAXS intensity increases during overcharge in three different regions. First, between 4 and 4.2 V as observed during the formation cycle, the SAXS intensity increases concomitantly with the H2 → H3 transition. From 4.2 to 5 V, the unit cell volume of LNO barely changes, while the SAXS intensity continues to increase. Interestingly, this voltage range is exactly where gas

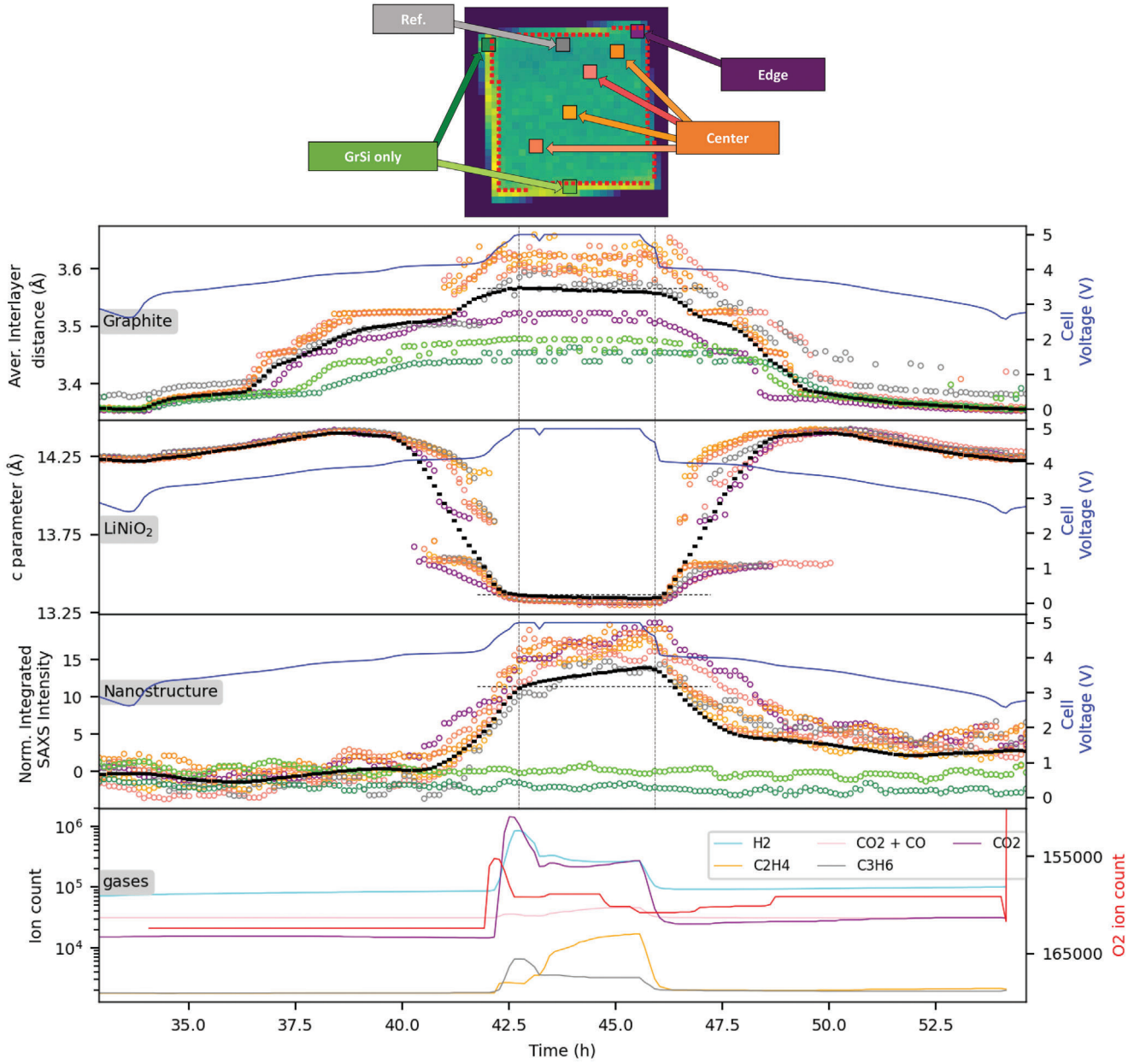

Figure 3. Structural changes and gas formation during the overcharge cycle. Evolution during overcharge of the interlayer distance in Li_xC_6, c parameter of Li_xNiO_2, SAXS integrated intensity, gas evolution for specific fragments. For all these graphs (apart for the gas analysis), different positions in the pouch cell are shown namely center, ref, edge, and GrSi only in orange, brown, purple, and green respectively. Black curve corresponds to the average over the entire electrode while the blue curve represents the full cell voltage profile. At the top of the graph, a transmission image of the pouch cell showing the selected positions in the pouch cell together with the borders of the LNO electrode (red dotted line). Horizontal lines at guide to the eyes to better appreciate to lattice parameter and SAXS intensity change during the hold at 5 V. Vertical grey dotted lines indicate the end of the charge (before the hold) and the beginning of the discharge.

evolution starts to increase massively. During the hold, the SAXS intensity continues to increase with a slower rate while the gas evolution rate also slows down. At the end of discharge, the intensity does not come back to its original value showing the irreversibility of some of the probed nanostructural changes. Analyzing quantitatively the SAXS signal is difficult, as it contains contributions from both anodic and cathodic materials, arising from large grains interfaces as well as nanosized objects. Moreover, it scales with volume fraction, specific surface, two-phase electronic contrast, and particle form factors. Nevertheless, the correlation between the observed LNO structural changes led us to formulate the following hypothesis: the SAXS intensity increase could be due to densification of the LNO due to (1) massive *c* parameter contraction during the H2 → H3 transition, and (2) the irreversible formation of densified surface layer due to O loss (See Supporting Information for more details).

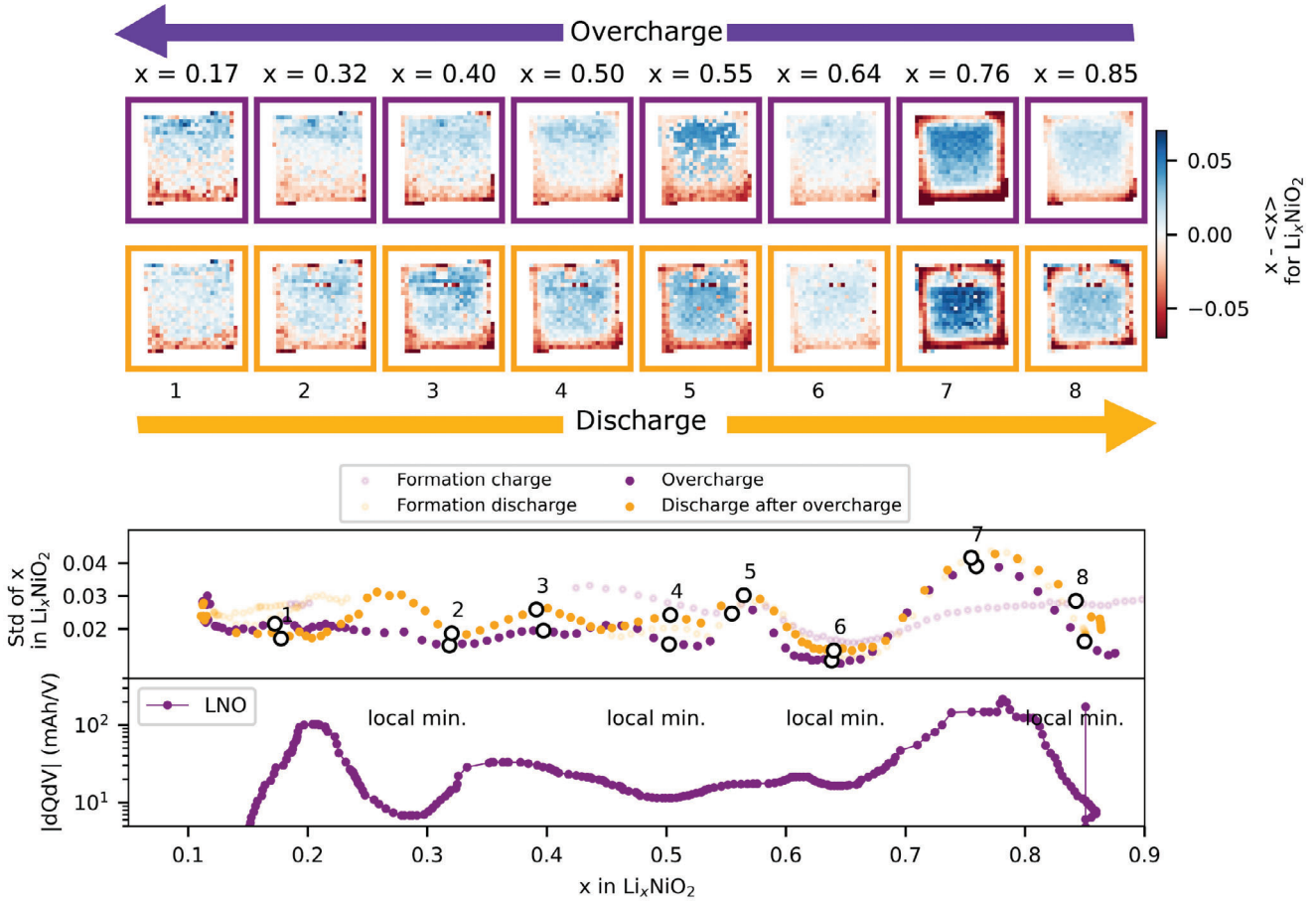

Figure 4. Reaction heterogeneity in LNO during overcharge and the discharge after overcharge. Top panel shows Li concentration deviation maps for the overcharge (top) and discharge after overcharge (bottom). Li concentration deviation maps are calculated by subtracting the spatial average across the entire electrode, <x>, from the local Li concentration, x, resulting in blue and red regions corresponding to zones having more and less Li compared to the average electrode. Maps are shown at key steps labeled 1 to 8, ranging from <x> = 0.85 to <x> = 0.17. The bottom panel shows the standard deviation of the Li concentration histogram for each maps which is a quantitative description of the amplitude of the spatial heterogeneity together with the dQ/dV of the overcharge cycle calculated for LNO. Purple colors are used for the charges and orange for the discharges. Note that the charge starts at $Li_{0.85}NiO_2$ due to Li loss in SEI formation during the formation cycle.

2.4. Effect of Overcharge on Spatial Li Concentration Heterogeneities

From the previous section, it appears that the average structural evolution of LNO and graphite during the discharge after overcharge is fairly similar to the discharge of the formation cycle, hence suggesting only minor impacts of overcharge on the reaction mechanism. To get more details about the effect of the overcharge, we analyze the spatial distribution of lithiation rates during and after the overcharge. Along that line, Li concentration maps in both electrode materials for all times have been produced based on lattice parameter variations. Briefly, a_{LNO} parameter is determined from both (101) and (003) reflections and used to estimate lithium concentration in LNO using the charge of the formation cycle and reference data from literature as calibration curves (Figures S15 and S16, Supporting Information).[15] On the graphite side, lithium concentration is estimated from both the phase fraction and interlayer distance of the different stages as reported earlier.[43] After obtaining dynamic lithium concentration maps, heterogeneity maps are produced by subtracting the spatial average from the local Li concentration ([Li] in a pixel) (**Figures** 4 and 5 for LNO and Gr respectively). Note that for graphite, the average Li concentration was not calculated over the entire electrode but over the electrode part directly facing LNO electrode. This allows better visualization of heterogeneities in the electrochemical stack by ruling out the effect of the oversized anode. In the following, we start by describing the heterogeneity of the lithiation rate followed by a discussion on the origin of such phenomena.

Focusing on the overcharge of LNO, the heterogeneity profile (spatial distribution of heterogeneity) depends on the state of charge and is visually maximum at approximately x = 0.75, as observed on the map at x = 0.76 (Figure 4a). For x ranging between 1 and 0.5 (x in Li_xNiO_2), electrode edges are always more delithiated (red) compared to the center of the pouch cell (blue). At higher SoC ($0 < x < 0.5$), the heterogeneities are weaker and the bottom edge of the pouch cell is the most delithiated zone. This edge was held down during the experiment and is also where the positive

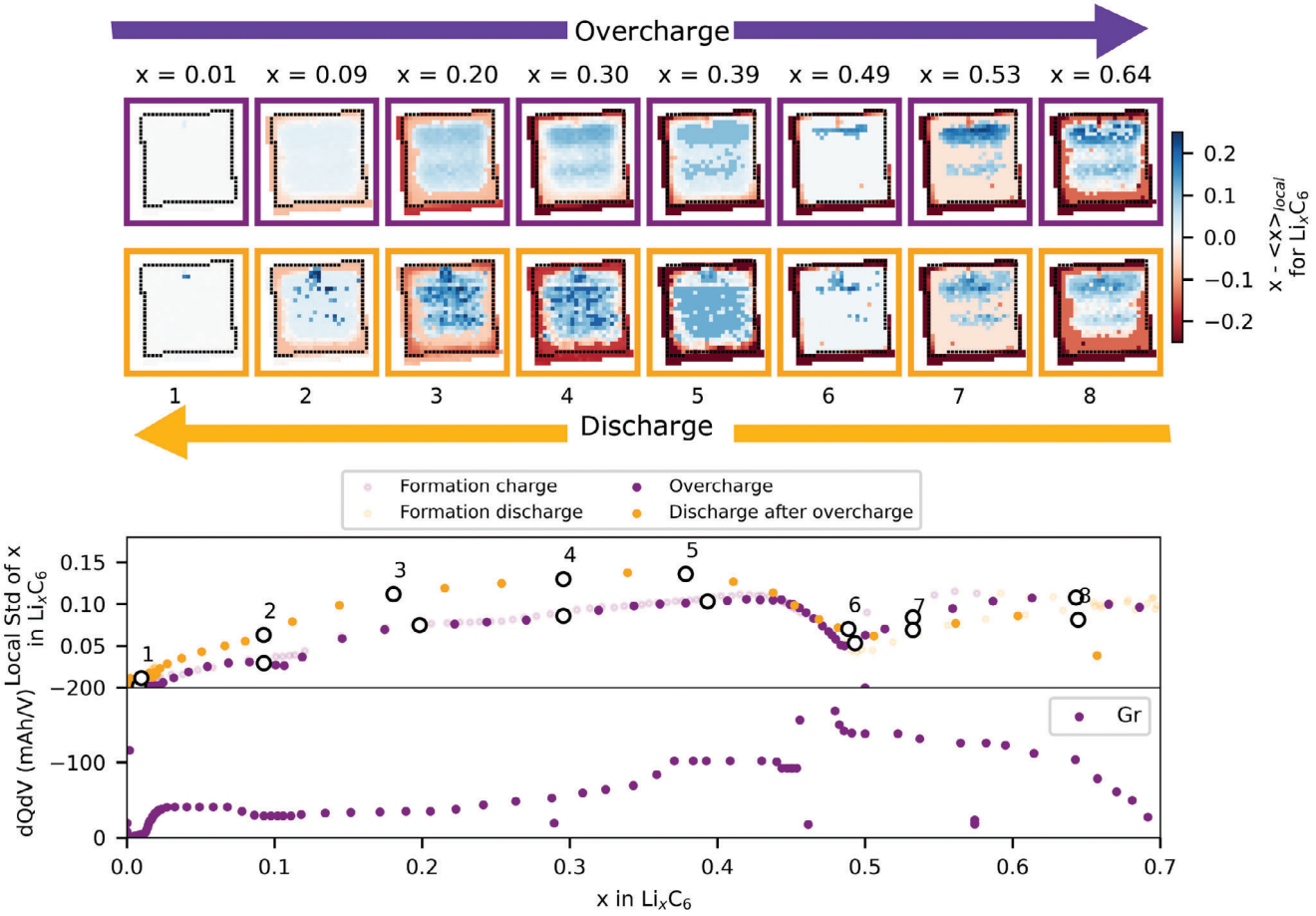

Figure 5. Reaction heterogeneity in graphite during overcharge and the discharge after overcharge. Top panel shows Li concentration deviation maps for the overcharge (top) and discharge after overcharge (bottom). Li concentration deviation maps are calculated as follows: for each pixel, the local Li concentration (of the pixel), x is subtracted the average Li concentration in the graphite electrode facing the LNO electrode, $\langle x \rangle_{local}$, resulting in red and blue regions corresponding to zones having more and less Li compared to the average electrode. The bottom panel shows the standard deviation of the Li concentration histogram for each maps which is quantitative description of the amplitude of the spatial heterogeneity – together with the dQ/dV of the overcharge cycle calculated for the Graphite–Silicon electrodes. Purple colors are used for the charges and orange for the discharges.

and negative tabs are located. It suggests that either electrolyte accumulation and/or shorter electronic diffusion pathways could results from lower overpotential hence early delithiation of LNO. At high state of charge, heterogeneities can be observed at the reference electrode position (blue dots at x = 0.32). During discharge after the overcharge, the general heterogeneity profile is similar to the charge (LNO in center of pouch cell is more lithiated compared to the edge) with however the presence of some very local heterogeneities not observed during overcharge and located at the center of the pouch cell, or close to the reference electrode position for example (visualized on Figure 4b as red pixels hence more delithiated areas). To quantitatively measure the intensity of the heterogeneities, standard deviation of the Li concentration histogram in the LNO electrode is shown in Figure 4c for all cycles. Apart from the 1st charge (See Figures S17 and S18, Supporting Information), the heterogeneity versus SoC curve shows several minima located approx. at x = 0.85, 0.65, 0.5, 0.3. Interestingly, there is a correlation between these minima and dQ/dV of LNO (Figure 4d) indicating that heterogeneities arise at voltage plateaus. Discharges have similar profiles and are more heterogeneous than the overcharge (i.e., shows a higher standard deviation value).

Turning to the graphite during overcharge (Figure 5), the heterogeneity profile clearly shows that graphite not facing LNO electrode displays a lower degree of lithiation (red). In the following, we focus on the heterogeneity of graphite facing LNO electrode (that is inside the black dotted line representing the LNO electrode contour in Figure 5). Generally, graphite is more lithiated (blue) in the center of the pouch cell with the exception of a broad horizontal line crossing the pouch cell. Lithiation difference between edges and center is SoC dependent, as it is stronger for example at x = 0.39 compared to x = 0.49. During discharge, the same heterogeneity pattern is observed with also very local heterogeneities appearing as speckles on map at x = 0.30 or blue dots at x = 0.09 located at the center of the pouch and reference electrode (more lithiated areas). On the standard deviation of the Li concentration histogram for the graphite directly facing LNO presented in Figure 5, it can be seen that (1) heterogeneity values are in average twice higher in graphite compared to LNO, (2) the heterogeneity depends on SoC with local minima at x ≈0.1, and

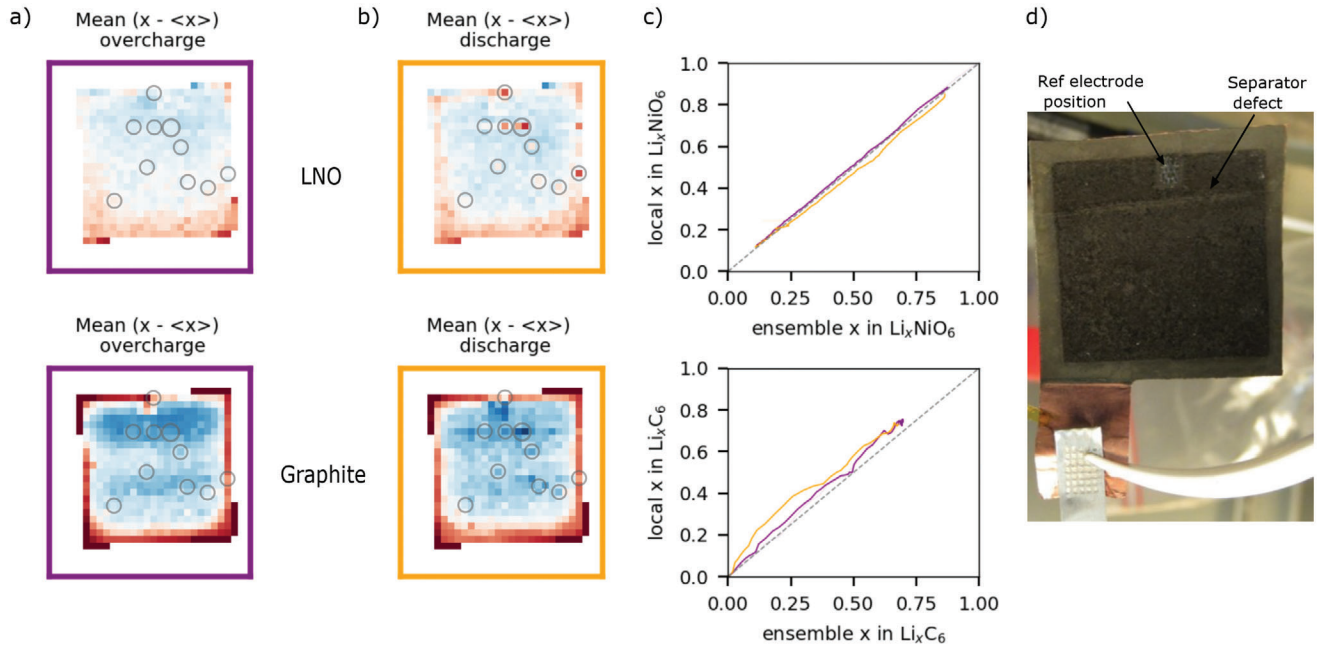

Figure 6. Overcharge-based local heterogeneities. a,b) are Li concentration deviation maps averaged over the entire overcharge and discharge, respectively (shown in purple and orange, respectively). Top and bottom maps are for LNO and graphite, respectively. All maps have dotted circles highlighting the position of heterogeneities observed during the overcharge. Dotted circles are the same for all conditions and sample. c) Electrode average Li concentration (ensemble x in Li_xNiO_2 and Li_xC_6 for the top and bottom panel, respectively) versus local Li concentration inside the circles shown in the maps a) and b). Purple and orange lines are for the overcharge and discharge, respectively. d) Picture of the dried and washed negative electrode after disassembling of the pouch with traces from the reference electrode and from the separator defect (line also visible on the separator after disassembling the cell).

0.5 somewhat matching the inflexion points in graphite electrochemical curve during lithiation (corresponding to pure Stage3L and Stage2), (3) the discharge after the overcharge is much more heterogeneous, especially for $0 < x < 0.4$.

We have shown that overcharge leads to local heterogeneities during the subsequent discharge. Interestingly, some of these local heterogeneities are found at the same positions on both positive and negative electrodes, as highlighted in **Figure 6**a,b. Moreover, by comparing Li concentration in LNO and graphite at these positions with electrode ensemble Li concentration (Figure 6c), it is clear that reactions at these positions are kinetically limited. Indeed, for LNO the local Li concentration during overcharge (purple line) matches the ensemble electrode lithiation as it follows the straight dashed lines (corresponding to $x_{local} = x_{ensemble}$). However, during the subsequent discharge, the local Li concentration (orange line) during the discharge deviate from the dashed line with the local concentration being smaller compared to the ensemble electrode concentration. For the graphite, local Li concentration during overcharging does not superimpose to the dashed line (due to the much larger heterogeneity observed in the graphite electrode compared to LNO), but the deviation to the ensemble Li concentration is even more pronounced during discharge. Note that before 5 V hold, (de)lithiation kinetics at these positions was closer to the ensemble electrode reaction confirming the detrimental effect of overcharge. Interestingly, the pouch cell was opened after the experiment and a visible defect was observed in the anode, which position matches some of the most pronounced damaged zones (Figure 6d).

3. Discussion

3.1. The Origin of the Heterogeneities

In summary, we evidence four heterogeneity effects: (1) graphite not facing LNO is under-lithiated, (2) there is frequently a delay of the reaction mechanism close to the reference which is presumably due to mechanical deformation leading to different current distribution (3) lithiation heterogeneity between the edges and the center of the electrodes is SoC dependent and occurs at every cycle, (4) there are local spots lagging behind the ensemble electrochemistry only present during the discharge after the overcharge.

First we want to discuss the effect of stack pressure on our observations. Stack pressure plays an important role at high C-rates because it limits Li inventory loss and modifies the electronic and ionic percolation.[44] However previous reports suggest it has a limited influence on the reaction heterogeneities at moderate C-rates.[25] Moreover, in this study relatively low C-rates were applied hence suggesting that stack pressure might not play a large role in the observed heterogeneities. Finally, heterogeneities n°1, 2, and 3 are mostly due to cell geometry and thermodynamics as detailed in the following paragraph. Regarding heterogeneity n°4, it is only present during the discharge following the overcharge, without change in the stack pressure.

We discuss the origin of the third and fourth type of heterogeneity which have very different characteristics. Regarding the SoC-dependent heterogeneity (n°3), the edges (4-5 mm) of LNO

are always more delithiated compared to the center of the pouch cell in charge or discharge, or during voltage holds. For graphite, the edges are also more delithiated during charge and discharge together with a broad line visible at the center of the pouch cell. These observations show that Li inventory (that is the sum of Li in cathode and anode) might not be spatially homogeneous over mm dimensions (in this case, area larger than the mm at the edges have less lithium compared to the center). Moreover, our observations also indicate that this type of in plane heterogeneity is not kinetically controlled but rather related to the shape of the voltage curve. To explain why both the LNO and graphite electrodes are under lithiated at the edges, we propose that Li extracted from LNO inserts over a large region in the graphite electrode (extending to graphite not directly facing LNO electrode), which leads to under-lithiated graphite. In turn, the under lithiated graphite electrochemical potential is higher which drives a higher electrochemical potential at the LNO electrode because full cell voltage is fixed. The raise of the electrochemical potential at the edges leads to lower Li concentration in LNO especially around flat voltage regions for which a small change in potential leads to large Li concentration change. This explains the SoC dependence of the heterogeneity. The fourth heterogeneity is only visible after the overcharge, and consists of very local spots which appear to be lagging behind the ensemble electrochemical reaction (in this case, slower delithiation for LNO and lithiation for graphite). Some of these local spots are visible for both electrodes while some are only observed on the graphite electrode – which seems more affected by overcharge based on the standard deviation values reported in Figures 4 and 5. For the spots present on both electrodes and matching the presence of visible separator defects, we believe the delay in the electrochemical reaction might be caused by gas bubbles gathering at these positions, coalescing, and pushing out the electrolyte, hence leading to higher resistance areas. Interestingly the rest of the LNO electrode does not seem to be affected by overcharge despite massive gas release and nanostructural modification at relatively slow C-rate used in this work. Graphite is more affected which is possibly correlated with the presence of C_2H_4 and H_2 suggesting SEI evolution on graphite surface. The heterogeneity induced by gas bubble formation has also been hypothesized by Charalambous et al. who monitored the lithiation heterogeneity during the formation cycle of NMC/Gr cell.[25] However, in their case, the heterogeneity is much more drastic since some regions of the anode remain unlithiated during charge. We hypothesize that the difference is due the evacuation of gases which occurs in our set-up.

3.2. Strength of Correlating Multiple Techniques and Perspectives

Here we discuss the strength of performing simultaneous multi-technique experiments by highlighting specific aspects from this work, discussing also potential future works as perspectives.

3.2.1. Reference Electrode Damage

We have observed a drift of the LFP/FP reference electrode potential during overcharge due to LFP delithiation (observed by WAXS mapping) in presence of CO_2 and O_2 (OEMS). This potential drift was not observed in pouches cycled in the lab. This is probably due to the vertical position of the pouch at ESRF leading to gas accumulation at the top of the cell where the reference electrode was positioned. The oxidation of LFP is difficult to reproduce and hence without the possibility to locally measure LFP/FP peak ratio with the x-rays, the data would have been discarded. Therefore, thanks to this multi-technique experiment, we have been able to understand that the potential drift has no influence on the validity of our dataset while questioning the chemical durability of non-active elements in batteries such as reference electrodes or sensors.

3.2.2. Reaction Mechanism

Phase transformation of LNO and Gr-Si electrodes are well known and some of the remaining debates are (1) the formation mechanism of the O1 phase, which is observed sometimes for low Ni anti-site defects materials and long hold at high voltage,[17] and (2) the respective contribution of graphite and Si in the electrochemical mechanism depending on the composite morphology.[14] We have shown the absence of O1 phase even after holding 3 h at 5V. Regarding the graphite/silicon composite mechanism, in this electrode, graphite reacts first during discharge in agreement with previous findings.[14] Gas production of both electrode separately is also well described in the literature, and are consistent with our results. $LiNiO_2$ at high voltage releases singlet O_2 chemically reacting with EC forming $H_2O_{(sol)}$, CO_2, and CO. While H_2O, EC, and FEC reduction on GrSi anode leads to H_2, C_2H_4, and CO_2 during the formation cycle. There is less consensus on the correlation between gas production and structure evolution, especially the onset of CO_2 and O_2 release using LNO electrodes. Some reports find O_2 and CO_2 before the H2→H3 transition [15,21] and others after.[42,45] We have observed CO_2 evolution only after the H2→ H3 transition. The important point to highlight here is that we have demonstrated on a well-known system that the multi-technique experiment is extremely powerful to study reaction mechanism in a single shot experiment. Applying this methodology to post Li-ion batteries such as Li-air or multivalent batteries in which there is no strong consensus on reaction mechanism would be extremely useful.

3.2.3. Gas production in Full Cell

Moving back to gas analysis, LNO/Gr-Si full cell gassing behavior during overcharge has not been studied previously. We found that overcharge leads to H_2, C_2H_4, C_3H_6, and CO_2 which are not expected from passivated Gr—Si electrode. This is in agreement with Michalak et al. who found that $LiNi_{0.5}Mn_{1.5}O_4$ (LNMO)/Gr full cell produce more gases than LNMO/LFP and LFP/graphite cells together showing the detrimental synergetic effect of combining LNMO and Gr electrodes.[46] What is the cross talk mechanism at play in our system? Schwenke et al. showed using OEMS on LFP/graphite cells that the presence of CO_2 gas during formation cycle reduce C_2H_4 production showing that CO_2 has a positive SEI builder effect on graphite surface.[47] Rinkel et al. identified and quantified soluble species analysing NMR spectra of electrolytes extracted from NMC/LFP, LFP/graphite and NMC/graphite cells.[38] The authors observed that some soluble species originating from cascade reaction of solvents or salt

with H_2O formed at the cathode side in NMC/LFP cells were not observed in NMC/Graphite. They concluded that H_2O preferentially reduce on the graphite anode modifying the SEI composition. HF produced from the oxidation of EC and $LiPF_6$ is also known to reduce on the anode side potentially damaging the SEI.[40] Mattinen et al. performed gas analysis on commercial NMC-LMO/Graphite cells and found the presence of C_2H_4 during charge.[48] Its concentration increases with C-rate suggesting Li plating, and hence re-formation of SEI, might be responsible for this observation. In our case, we do not have Li plating anywhere in the cell as confirmed by the absence of Li metal diffraction peaks and consistent with the oversized anode. Note that WAXS mapping is especially useful to detect local Li plating as demonstrated by Paul et al.[22] Therefore, in light of literature, we believe that HF and/or H_2O created at the cathode migrates to the anode and reduces forming H_2 while degrading the SEI structure exposing novel graphite surface, and hence leading to further electrolyte reduction leading to the formation of C_2H_4. Interestingly, C_2H_4 signal only decreases after the end of hold suggesting a continuous decomposition of the SEI during the hold. Future work could be devoted to study the SEI using this multi-technique experiment, in particular by making use of SAXS to unveil the nanoscale morphological changes and nature of nanosized interfacial regions. Indeed, small angle neutron scattering has been used to characterise the SEI morphology on Si anodes cycled in deuterated electrolyte taking advantage of the strong scattering cross section difference between protonated and deuterated materials. Adopting this methodology with SAXS could be possible if a contrasting agent was introduced in the electrolyte.

3.2.4. Gas Imaging

There are reports directly imaging gas bubbles inside cells. Sun et al. used μX-ray computed tomography (CT) on small Swagelok-type cells and found gas accumulation in the pores of a Si anode.[49] Du et al. performed lab X-ray CT on a commercial prismatic cell and observed gas accumulating at the electrode/separator interface during cycling.[50] Finally, Michalak et al. using neutron imaging on a single layer pouch cell and measured gas accumulation mostly outside of the electrode stack, in the cell "headspace".[50] Therefore, depending on the cell geometry, gas is found in and/or out of the electrode stack. Trapped gas in the electrode stack could be deleterious for cell behavior, in particular to cause impedance rise and capacity loss. We have shown that overcharge produces local spots featuring kinetically limited (de)lithiation reactions possibly due to trapping of gas bubbles localized close to cell manufacturing defects. These findings are complementary to previous observations because our technique, which is not directly sensitive to the presence of gas, informs on the electrochemical lag, which might be induced by the presence of gas. To support the presence of bubbles, we can compare the amount of gas released during the overcharge in our system with results originating from other cell designs in which gas trapping is less likely. Sim et al. have developed a flooded cell, and measured the gassing behavior of $LiNiO_2$ up to 4.8 V.[45] They found 341 μmol g^{-1}_{LNO} of gasses was released during the full electrochemical sequence. In our case, we found 250 μmol g^{-1}_{LNO} (Figure S12, Supporting Information), which is on the same order of magnitude but lower. The amount of gases produced depends on many factors such as the surface area, the electrolyte and the presence of trapped gas. Our particles are slightly smaller compared to Sim et al., and the electrolyte composition differs (LP57 compared to pure EC with $LiPF_6$)i It is thereby difficult to be conclusive, but the smaller amount of gas measured in our case is consistent with the presence of trapped bubbles. To keep investigating the fate and effect of gas trapped in the electrode stacks, a possible development of this experiment could be to use a commercial prismatic cell instead of a single pouch cell. Extra lab-XCT experiment could be performed after the synchrotron experiment to localise the gas bubbles and hence make a direct correlation between their presence and their effect on the reaction mechanism observed by *operando* WAXS mapping.

4. Conclusion

In this work, we have demonstrated the proof of concept of an *operando* multi-probe experiment producing high-quality and correlated WAXS/SAXS mapping together with gas evolution data during formation and overcharge of $LiNiO_2$/Gr—Si single layer pouch cell without beam damage effect on any of the datasets. Correlative analysis of the datasets provides a series of new insights on overcharge mechanism namely (1) massive gas release from the LNO can be observed without substantial O1 phase formation, (2) evolved gasses can react with cell components (oxidizing the LFP or Graphite–Silicon electrode) questioning the general perspective on the chemical durability of sensors in battery, (3) overcharge leads to substantial gas release from the anode even if it is not fully lithiated and in absence of Li plating showing the importance of cross talks reactions, (4) defects, tabs, reference electrode, and wrong local electrode balancing introduce heterogeneous reactions which need to be taken into consideration for thermal and/or ageing simulations, and (5) as opposed to formation cycle, overcharge produces local spots featuring kinetically limited (de)lithiation reactions possibly due to trapping of gas bubbles in cell manufacturing defects. This correlative method can be applied to investigate more severe overcharging conditions and/or high temperatures, as requested for battery homologation. It would be particularly interesting to follow Ni-rich materials thermal stability in a variety of usage or abusive conditions, as it is directly linked to crystal changes and oxygen release. Moreover, our results emphasize the importance of controlling internal defects that may induce thermal, mechanical, and electrical heterogeneities affecting local chemistry and electrochemical redox reactions. Homogeneous cell designs optimizing tabs location, or smart cells built with miniaturized gas sensors and stable reference electrode, together with chemistry tuning (Ni-rich coating, electrolyte,...), appear to be key to limit gassing and avoid the local increase of internal resistance, inducing local overheating and over(de)lithiation, and potentially leading to safety issues. Coupling the OEMS-SAXS/WAXS set-up to other probes, particularly to chemical-sensitive techniques capable to measure soluble species or interfacial compounds, would be the next step to integrate knowledge from electrochemistry, structure, gas generation, and chemical environment measures for an integral characterization of full cells. Applying the method to large-scale

formats as prismatic or cylindrical cells, and also integrating computed tomography options, could also leverage our understanding of the origin of defects and localized degradations.

5. Experimental Section

Pouch Cell: Single layer pouch cells are assembled using $LiNiO_2$ electrode (94%wt. active material, 3%wt. C65, 3%wt. PVDF – BASF) and Gr—Si electrode (85% wt of active material including 11% wt of Si nanoparticles – CIDETEC). Electrode capacity loadings are 3 and 3.3 mAh.cm^{-2}, respectively. The separator is two layers of DreamWeaver Gold, non-woven sheet made of Kevlar-type fibers, and the electrolyte is 1.3 M $LiPF_6$ in ethylene carbonate (EC) and 10 wt.% fluoroethylene carbonate (FEC). Organic carbonate solvents with high vapor pressures such as dimethyl carbonate (DMC) and ethyl methyl carbonate (EMC) were not used in this study to prevent the mass-spectrometer contamination. The separator was chosen to ensure good wettability with the electrolyte. The cell was assembled in a dry room with a dew point of −40 °C and all the components were dried prior to assembly at 105 °C in vacuum for 24h. The electrode area was 2.3 × 2.3 cm^2 for LNO and 2.7 × 2.7 cm^2 for Gr—Si while the separator was larger to prevent short circuit (4.0 × 4.0 cm). The negative versus positive capacity ratio (N/P) is 1.51. This is calculated considering the total capacity of the electrode taking into account their size and capacity loading. The reference electrode is partially delithiated $LiFePO_4$ (LFP) of ≈0.2 × 0.2 cm size. It was electrochemically pre-delithiated to achieve a LFP/FP phase fraction of 1/1 to ensure stable electrochemical potential of 3.42 V versus Li/Li$^+$. The reference electrode was inserted between the cathode and the anode and electrically insulated by a layer of separator on each side. 1/32″ diameter PEEK tubes were sealed in the pouch cell using a thermosealing polymer, and served as gas inlet and outlet for the cell. Positive Al and negative Cu tabs were also sealed in the pouch cell using thermosealing polymer. After activation and vacuum-sealing, the cell was wetted in a "flat state" during 6 h prior to connection to the gas analysis line. After assembly, the pouch cell was pressed between two glassy carbon windows (4 × 4 cm^2 and 0.5 mm thick) using stainless steel perforated plates and clips. The accessible area for SAXS/WAXS observations was 3 × 3 cm^2. A picture of the cell and a schematic view of the investigated electrode stack are presented in Figure S1 (Supporting Information). Electrochemical cycling of the pouch cell was performed using a SP-300 potentiostat (BioLogic) in galvanostatic and potentiostatic modes by controlling the cell voltage while measuring both positive and negative electrode potentials against the reference electrode. One formation cycle was performed at C/13 with cut-off voltages of 4.2 and 2.5 V versus Li/Li$^+$ with a potentiostatic hold at the end of charge at 4.2 V until reaching C/50 current. The hold ending conditions were achieved by either limiting the current to 0.24 mA or the step time to 2h. The overcharge cycle was then performed at C/9 with cut-off voltages of 5.0 – 2.5 V and a 3 h hold at 5 V at the end of overcharge. Note that the hold was interrupted after 30 min for a short rest time in open circuit voltage (OCV) of 7 min. The temperature during the tests was 26 °C measuring at a temperature sensor placed against of external casing of the pouch.

Gas Analysis: The pouch cell was mounted on the BM02 beamline at the European Synchrotron Radiation Facility (ESRF, Grenoble, France). The OEMS technique was applied to analyze the gases released during the electrochemical test of the pouch cell. For that purpose, a gas analysis line containing mostly 1/8″ metallic tubes was built-up around the cell. Ultrapure Ar BIP (>99.9999%) was used as a carrier gas. A gas purification column was installed before the electrochemical cell to remove any possible residual impurities from the tubing. A digital mass-flow controller was used to supply a constant flow of Ar of 2 mL.min^{-1} to the cell. The gas analysis line was equipped with a vacuum pump and a bypass to be able to clean/purge the tubing prior to passing the gas through the cell. Flexible 1/32″ PEEK tubing sealed into the cell from both sides (Figure S1a, Supporting Information) allowed a non-interrupted gas flow through the cell during its continuous movement. The pressure in the gas analysis line was 1098 mbar(a) during the experiment. Hiden HPR20 S1000 triple filter quadrupole mass spectrometer with pulse ion counting electron multiplier detector was used for the measurements. The cell was purged with Ar for 3 h for stabilization of baseline gas signals before starting the electrochemical test. The following mass-to-charge ratio (m/z) values were measured in Multiple Ion Detection mode: 44 (CO_2), 2 (H_2), 28 (CO+C_2H_4 mostly with minor contribution from CO_2), 29 (CO + C_2H_4 mostly), 32 (O_2), 15 (CH_4), 41 (C_3H_6). The volume of the electrochemical cell was 10 mL, giving a response time for OEMS analysis of 5 min. No calibration with a standard gas bottle was conducted during the experiment due to restricted beam time. However, the tests were repeated later in the laboratory for comparison with a gas quantification (Figure S11, Supporting Information).

GC-MS measurements were conducted with an Agilent 7890A system using a J&W DB-200 122–2032 column. Injection occurred in split mode at 280 °C with 1 µL of sample carried by He gas with a 120 mL·min^{-1} flow rate. The column temperature ramp started at 40 ° until 200 °C at 10 °C min^{-1}. The mass analyzer was a MSD5975C (Agilent) with electron impact ionization.

SAXS/WAXS Mapping: SAXS/WAXS mapping was performed on the French beamline BM02 at the European Synchrotron Radiation Facility (ESRF). Dataset can be found on the ESRF data portal using the following link https://doi.esrf.fr/10.15151/ESRF-ES-1058211918. A 65 × 100 µm^2 beam at 18 keV with 1.9e10 photons s^{-1} was used (λ = 0.6888 Å). During the acquisition, the pouch cell was moved horizontally (x) and vertically (y) to scan the entire electrode surface, producing (x, y) maps of 31 × 31 pixels with pixel size of 1 mm in ≈6 min. As the SAXS and WAXS modalities are available simultaneously by using two detectors, each pixel contained a WAXS and a SAXS pattern. To reach this time resolution, "horizontal fly scans" were performed in which the pouch cell was continuously moved in the *x* direction from 0 to 31 mm while the shutter remained opened. Detector images were averaged over 1 mm pouch cell displacement. Therefore, each detector image was an average in the *x* direction of 1 mm of the sample. After every horizontal continuous scan, the pouch cell was displaced vertically by 1 mm (in y direction) and a new continuous scan in *x* was performed until the full 2D maps were produced. Dose calculations using Jousseaume et al. work were performed and gave 85 kGy and 2 kGy for the cathode and anode, respectively, which is below the estimated threshold for beam damage.[51] WAXS patterns were recorded using an imXPAD WOS detector, while the SAXS was recorded on an imXPAD S540 detector placed 11.6 and 3544 mm behind the sample, respectively. Sample-to-detector distance calibration was performed using reference materials: silver behenate ($AgC_{22}H_{43}O_2$) for SAXS and lanthanum hexaboride (LaB_6) for WAXS. Azimuthal integration was performed using PyFAI[52] and the patterns were normalized by I_o (incoming photon flux) and I_t (transmitted photon flux). Continuous acquisition was performed during the electrochemical cycling. Note that two detector shut-downs occurred during the formation cycle (middle of charge and of discharge) and provoked the absence of scattering data in these corresponding time lapse. After obtaining the WAXS patterns, data was re-calibrated to correct for the (small) difference in position between the LaB_6 reference and the electrode in the pouch cell. Calibration was performed pixel by pixel using Cu peak position as a reference using the formulas below in which, Q_{obs}, $Q_{th,}$ and λ are the observed peak position before calibration, the theoretical value, and the wavelength.

$$Q_{new} = \frac{4\pi}{\lambda} * \sin\left(\frac{1}{2} * \tan^{-1}\left(\frac{1}{K * \tan\left(2 * \sin^{-1}\left(\frac{\lambda * q * \pi}{4}\right)\right)}\right)\right) \quad (1)$$

where K is defined by:

$$K = \frac{\tan\left(2 * \sin^{-1}\left(\frac{\lambda * Q_{obs} * \pi}{4}\right)\right)}{\tan\left(2 * \sin^{-1}\left(\frac{\lambda * Q_{th} * \pi}{4}\right)\right)} \quad (2)$$

Cu peak is a good choice because (1) it is intense, (2) it is spatially close to the anode and the cathode, and (3) it is present everywhere in

the pouch allowing for a proper calibration of the data even if the pouch would not be locally straight or completely flat. Indeed, in this case, there is a small angle between the plane of the pouch and the detector plane, as observed from the variation of the Cu peak position in $Å^{-1}$ as a function of its position in the pouch (Figure S19, Supporting Information). Cu peak position varies by less than 5e-4 $Å^{-1}$ during the electrochemical sequence showing that the pouch does not change position with time. Therefore, it is not necessary to have a time-dependent calibration of the Q range. Background removal was performed using Prisma[53] which uses symmetric Least-Squares smoothing method (AsLS) developed by Eilers and Boelens.[54] Moreover, peaks that did not evolve during the formation cycle and overcharge were considered as background and subtracted from the patterns. To get Li concentration in $LiNiO_2$, the centers of mass of (003) and (101) Bragg reflections were determined for every WAXS pattern and used to determine *a* and *c* lattice parameters. Center of mass formula is the following with Q1, Q2, I(Q), and I_{tot}, the value of Q before the peak, the value of Q after the peak, the intensity profile as a function of Q, and the integral of the intensity between Q1 and Q2:

$$Center\ of\ mass = \sum_{Q1}^{Q2} Q * \frac{I(Q)}{I_{tot}} \quad (3)$$

The Li concentration versus *a* lattice parameter calibration curve was fitted using charge of formation cycle and reference data,[15] and used to convert *a* into Li concentration (See Figures S15 and S16, Supporting Information). To determine Li concentration in graphite electrode, the relative intensity and center of mass of peaks in the 1.91 – 1.838, 1.837 – 1.805, 1.8 – 1.761 and 1.73 – 1.66 $Å^{-1}$ regions, respectively corresponding to graphite, Stage 3, Stage 2/2L and Stage 1 (LiC_6) transitions were determined.[28] The Li concentration of each phase is determined based on the peak center of mass following the work of S. Tardif et al.[43] The overall Li concentration in graphite at every pixel position was obtained by averaging over the different phases weighted by their respective phase fractions calculated by the relative peak intensities. (111) Bragg reflection of crystalline silicon is observed in the WAXS pattern and used to qualitatively determine changes in crystalline Si amount. Radially-averaged 1D SAXS data mostly consist of a decaying intensity, without significant shape change during the electrochemical sequence, hence it was integrated between 4.10^{-3} and 3.10^{-2} $Å^{-1}$ to follow the averaged integrated intensity variations.

Supporting Information

Supporting Information is available from the Wiley Online Library or from the author.

Acknowledgements

Beamtime at the ESRF was granted within the Battery Pilot Hub MA4929 "Multi-scale Multi-techniques investigations of Li-ion batteries: toward a European Battery Hub". The authors acknowledge support from the EU H2020 project BIG-MAP (grant agreement ID: 957189). The authors are grateful to J.F. Martin for conducting post-mortem GC-MS analysis of the electrolytes and to D. Buzon for fruitful discussions.

Conflict of Interest

The authors declare no conflict of interest.

Author Contributions

Q.J. and I.P. contributed equally to this work. Q.J. and I.P. conceived the idea. S.L. supervised the project. Q.J., S.T., and S.L. designed the synchrotron experiment. I.P., L.B., E.A., B.A., and P.C. prepared the samples and performed the lab-scale experiments. N.B. aligned and set the beamline. All authors participated to the beamtime except of L.D. I.P., and L.B. analyzed the gas data, Q.J. and S.L. analyzed X-ray data, Q.J., I.P. L.B. wrote the manuscript, L.D. and S.L. revised the manuscript, all authors discussed the results and contributed to the manuscript.

Data Availability Statement

The data that support the findings of this study are available from the corresponding author upon reasonable request.

Keywords

Li-ion battery, *operando* characterization, synchrotron

Received: September 6, 2024
Revised: November 19, 2024
Published online:

[1] O. Vidal, B. Goffé, N. Arndt, *Nat. Geosci.* **2013**, *6*, 894.
[2] R. Herrington, *Nat. Rev. Mater.* **2021**, *6*, 456.
[3] M. Bianchini, M. Roca-Ayats, P. Hartmann, T. Brezesinski, J. Janek, *Angew. Chem., Int. Ed.* **2019**, *58*, 10434.
[4] Z. Cui, A. Manthiram, *Angew. Chem., Int. Ed.* **2023**, *62*, 202307243.
[5] R. Pan, E. Jo, Z. Cui, A. Manthiram, *Adv. Funct. Mater.* **2023**, *33*, 2211461.
[6] K. Kalaga, M.-T. F. Rodrigues, S. E. Trask, I. A. Shkrob, D. P. Abraham, *Electrochim. Acta* **2018**, *280*, 221.
[7] M. Metzger, B. Strehle, S. Solchenbach, H. A. Gasteiger, *J. Electrochem. Soc.* **2016**, *163*, A798.
[8] S. Müller, J. Eller, M. Ebner, C. Burns, J. Dahn, V. Wood, *J. Electrochem. Soc.* **2018**, *165*, A339.
[9] J. B. Quinn, T. Waldmann, K. Richter, M. Kasper, M. Wohlfahrt-Mehrens, *J. Electrochem. Soc.* **2018**, *165*, A3284.
[10] L. Zhang, L. Huang, Z. Zhang, Z. Wang, D. D. Dorrell, *Appl. Energy* **2022**, *327*, 120026.
[11] S. J. Edge, S. O'Kane, R. Prosser, D. N. Kirkaldy, N. A. Patel, A. Hales, A. Ghosh, W. Ai, J. Chen, J. Yang, S. Li, M.-C. Pang, L. B. Diaz, A. Tomaszewska, W. M. Marzook, N. K. Radhakrishnan, H. Wang, Y. Patel, B. Wu, J. G. Offer, *Phys. Chem. Chem. Phys.* **2021**, *23*, 8200.
[12] D. Atkins, E. Capria, K. Edström, T. Famprikis, A. Grimaud, Q. Jacquet, M. Johnson, A. Matic, P. Norby, H. Reichert, J.-P. Rueff, C. Villevieille, M. Wagemaker, S. Lyonnard, *Adv. Energy Mater.* **2022**, *12*, 2102694.
[13] J. I. G. Dawkins, I. Martens, A. Danis, I. Beaulieu, D. Chhin, M. Mirolo, J. Drnec, S. B. Schougaard, J. Mauzeroll, *Joule* **2023**, *7*, 2783.
[14] C. L. Berhaut, D. Z. Dominguez, P. Kumar, P.-H. Jouneau, W. Porcher, D. Aradilla, S. Tardif, S. Pouget, S. Lyonnard, *ACS Nano* **2019**, *13*, 11538.
[15] L. de Biasi, A. Schiele, M. Roca-Ayats, G. Garcia, T. Brezesinski, P. Hartmann, J. Janek, *ChemSusChem* **2019**, *12*, 2240.
[16] P.-H. Chien, X. Wu, B. Song, Z. Yang, C. K. Waters, M. S. Everett, F. Lin, Z. Du, J. Liu, *Batteries Supercaps* **2021**, *4*, 1701.
[17] C. Xu, P. J. Reeves, Q. Jacquet, C. P. Grey, *Adv. Energy Mater.* **2021**, *11*, 2003404.
[18] L. Croguennec, C. Pouillerie, A. N. Mansour, C. Delmas, *J. Mater. Chem.* **2001**, *11*, 131.
[19] K. Park, Y. Zhu, C. G. Torres-Castanedo, H. J. Jung, N. S. Luu, O. Kahvecioglu, Y. Yoo, J. T. Seo, J. R. Downing, H. Lim, M. J. Bedzyk, C. Wolverton, M. C. Hersam, *Adv. Mater.* **2022**, *34*, 2106402.
[20] R. Sim, J. Langdon, A. Manthiram, *Small Methods* **2023**, *7*, 2201438.
[21] M. Juelsholt, J. Chen, A. M. Pérez-Osorio, J. G. Rees, S. D. S. Coutinho, E. H. Maynard-Casely, J. Liu, M. Everett, S. Agrestini, M.

Garcia-Fernandez, K.-J. Zhou, A. R. House, G. P. Bruce, *Energy Environ. Sci.* **2024**, *17*, 2530.
[22] P. P. Paul, V. Thampy, C. Cao, H.-G. Steinrück, R. T. Tanim, R. A. Dunlop, J. E. Dufek, E. S. Trask, N. A. Jansen, F. M. Toney, J. N. Weker, *Energy Environ. Sci.* **2021**, *14*, 4979.
[23] K. V. Graae, X. Li, D. R. Sørensen, E. Ayerbe, I. Boyano, D. Sheptyakov, M. R. V. Jørgensen, P. Norby, *J. Power Sources* **2023**, *570*, 232993.
[24] P. D. Finegan, A. Quinn, S. D. Wragg, M. A. Colclasure, X. Lu, C. Tan, M. Heenan, M. T., R. Jervis, L. Brett, D. J., S. Das, T. Gao, A. D. Cogswell, Z. M. Bazant, M. D. Michiel, S. Checchia, R. P. Shearing, K. Smith, *Energy Environ. Sci.* **2020**, *13*, 2570.
[25] H. Charalambous, D. P. Abraham, A. R. Dunlop, S. E. Trask, A. N. Jansen, T. R. Tanim, P. R. Chinnam, A. M. Colclasure, W. Xu, A. A. Yakovenko, O. J. Borkiewicz, L. C. Gallington, U. Ruett, K. M. Wiaderek, Y. Ren, *J. Power Sources* **2021**, *507*, 230253.
[26] M. Wetjen, S. Solchenbach, D. Pritzl, J. Hou, V. Tileli, H. A. Gasteiger, *J. Electrochem. Soc.* **2018**, *165*, A1503.
[27] F. Larouche, K. Amouzegar, G. Houlachi, P. Bouchard, G. P. Demopoulos, *J. Electrochem. Soc.* **2022**, *169*, 073509.
[28] C. Didier, W. K. Pang, Z. Guo, S. Schmid, V. K. Peterson, *Chem. Mater.* **2020**, *32*, 2518.
[29] T. Jousseaume, J.-F. Colin, M. Chandesris, S. Lyonnard, S. Tardif, *Energy Environ. Sci.* **2024**, *17*, 2753.
[30] C. L. Berhaut, M. Mirolo, D. Z. Dominguez, I. Martens, S. Pouget, N. Herlin-Boime, M. Chandesris, S. Tardif, J. Drnec, S. Lyonnard, *Adv. Energy Mater.* **2023**, *13*, 2301874.
[31] B. Rowden, N. Garcia-Araez, *Energy Rep.* **2020**, *6*, 10.
[32] R. Jung, M. Metzger, F. Maglia, C. Stinner, H. A. Gasteiger, *J. Electrochem. Soc.* **2017**, *164*, A1361.
[33] L. A. Kaufman, B. D. McCloskey, *Chem. Mater.* **2021**, *33*, 4170.
[34] L. J. Krause, T. Brandt, V. L. Chevrier, L. D. Jensen, *J. Electrochem. Soc.* **2017**, *164*, A2277.
[35] L. D. Ellis, J. P. Allen, L. M. Thompson, J. E. Harlow, W. J. Stone, I. G. Hill, J. R. Dahn, *J. Electrochem. Soc.* **2017**, *164*, A3518.
[36] S. E. Sloop, J. B. Kerr, K. Kinoshita, *J. Power Sources* **2003**, *119–121*, 330.
[37] K. Märker, P. J. Reeves, C. Xu, K. J. Griffith, C. P. Grey, *Chem. Mater.* **2019**, *31*, 2545.
[38] B. L. D. Rinkel, J. P. Vivek, N. Garcia-Araez, C. P. Grey, *Energy Environ. Sci.* **2022**, *15*, 3416.
[39] L. Xia, B. Tang, L. Yao, K. Wang, A. Cheris, Y. Pan, S. Lee, Y. Xia, G. Z. Chen, Z. Liu, *ChemistrySelect* **2017**, *2*, 7353.
[40] S. Solchenbach, M. Metzger, M. Egawa, H. Beyer, H. A. Gasteiger, *J. Electrochem. Soc.* **2018**, *165*, A3022.
[41] V. Etacheri, O. Haik, Y. Goffer, G. A. Roberts, I. C. Stefan, R. Fasching, D. Aurbach, *Langmuir* **2012**, *28*, 965.
[42] J. K. Papp, N. Li, L. A. Kaufman, A. J. Naylor, R. Younesi, W. Tong, B. D. McCloskey, *Electrochim. Acta* **2021**, *368*, 137505.
[43] S. Tardif, N. Dufour, J.-F. Colin, G. Gébel, M. Burghammer, A. Johannes, S. Lyonnard, M. Chandesris, *J. Mater. Chem. A* **2021**, *9*, 4281.
[44] C. Cao, H.-G. Steinrück, P. P. Paul, A. R. Dunlop, S. E. Trask, A. N. Jansen, R. M. Kasse, V. Thampy, M. Yusuf, J. N. Weker, B. Shyam, R. Subbaraman, K. Davis, C. M. Johnston, C. J. Takacs, M. F. Toney, *J. Electrochem. Soc.* **2022**, *169*, 040540.
[45] R. Sim, A. Manthiram, *Adv. Energy Mater.* **2024**, *14*, 2303985.
[46] B. Michalak, H. Sommer, D. Mannes, A. Kaestner, T. Brezesinski, J. Janek, *Sci. Rep.* **2015**, *5*, 15627.
[47] K. U. Schwenke, S. Solchenbach, J. Demeaux, B. L. Lucht, H. A. Gasteiger, *J. Electrochem. Soc.* **2019**, *166*, A2035.
[48] U. Mattinen, M. Klett, G. Lindbergh, R. Wreland Lindström, *J. Power Sources* **2020**, *477*, 228968.
[49] F. Sun, H. Markötter, I. Manke, A. Hilger, N. Kardjilov, J. Banhart, *ACS Appl. Mater. Interfaces* **2016**, *8*, 7156.
[50] W. Du, R. E. Owen, A. Jnawali, T. P. Neville, F. Iacoviello, Z. Zhang, S. Liatard, D. J. L. Brett, P. R. Shearing, *J. Power Sources* **2022**, *520*, 230818.
[51] T. Jousseaume, J.-F. Colin, M. Chandesris, S. Lyonnard, S. Tardif, *ACS Energy Lett.* **2023**, *8*, 3323.
[52] J. Kieffer, D. Karkoulis, *J. Phys.: Conf. Ser.* **2013**, *425*, 202012.
[53] E. Flores, N. Mozhzhukhina, X. Li, P. Norby, A. Matic, T. Vegge, *Chem. Methods* **2022**, *2*, 202100094.
[54] P. H. C. Eilers, *Anal. Chem.* **2003**, *75*, 3631.